

Alternative Electron Models of an FFAG Muon Accelerator

E. Keil

Abstract

Parameters are derived for the lattice and RF system of two electron models of a non-scaling FFAG ring for accelerating muons. Both models accelerate electrons from about 10 to 20 MeV. Lattice parameters such as magnet types and dimensions, spacings, and number of cells are presented. The model circumferences are about 11 and 17 meters, respectively, and the magnet apertures are 12 mm × 18 mm. The parameters of the magnetic components are compared to those of existing magnets. The tune variation with momentum is similar to that in a full machine and would allow the study of resonance crossing. The consequences of misaligned magnets are studied by simulation. The variation of orbit length with momentum is less than 36 mm and would allow the study of acceleration outside a bucket. A 100 mm straight section, in each of the cells, is adequately long for an RF cavity operating at 3 GHz. The accelerating voltage needed is calculated. Practical RF system design issues, e.g. RF power, and the limit on the bunch population due to beam loading are estimated.

Geneva, Switzerland

February 10, 2004

1 Introduction

This brief note discusses two electron models for a non-scaling FFAG ring accelerating muons. Keil and Sessler have already presented a similar electron model with 33 periods [1]. Its lattice parameters were close to those circulated by J.S. Berg [2] at the FFAG Workshop, held from 13 to 17 October 2003 at BNL. It had about 11 m circumference, and accelerated electrons from 10 to 20 MeV. The two lattices in this note consists of 36 and 45 periods, respectively. The periods are 0.3 m and 0.38 m long, respectively. Focusing is by a triplet of combined-function dipoles. The practical realization of such dipoles is discussed, and their parameters are compared to those of existing magnets. Each period includes a straight section of 0.1 m length, which is long enough to house an RF cavity that operates at about 3 GHz and is half an RF wavelength long. The accelerating voltage needed is calculated. Practical RF system design issues, e.g. RF power, and the limit on the bunch population due to beam loading are estimated.

Table 1: Parameters of two electron model lattices at the reference energy 15 MeV

Number of cells	36	45	
Cell length	0.3	0.38	m
F magnet length	30	50	mm
F magnet angle	-64.894	-37.459	mrads
F magnet gradient	12.835	5.638	T/m
F magnet field	-108.168	-37.464	mT
D magnet length	100	100	mm
D magnet angle	304.320	214.545	mrads
D magnet gradient	-6.465	-4.746	T/m
D magnet field	152.177	107.285	mT
File	nov26b	dec06f	

2 Electron Model Lattice Parameters

Tab. 1 shows the main parameters of the electron model lattices. In the first new lattice, the number of periods is increased from 33 to 36 in order to move the vertical tune at the reference energy away from an integral value. The second new lattice is designed with longer horizontally focusing dipoles, in order to increase the ratio of their effective magnetic length and their aperture and to reduce their gradient. Also more space is provided between the dipoles in the triplet for the

coils. The increased period length is compensated by increasing their number, in order to keep the path length variation approximately constant. In both lattices, two horizontally focusing gradient dipoles surround a horizontally defocusing gradient dipole. The distances between the dipoles in the triplet are 20 and 40 mm, respectively. The combined-function dipoles are assumed to be rectangular magnets. Rectangular magnets have parallel end faces, and the reference trajectory enters and leaves them at an angle. One would naively expect that increasing the number of periods from 36 to 45 would decrease the bending angles in the ratio $36/45 = 4/5$. Tab. 1 shows that both bending angles are reduced much more, in particular the reverse deflection in the F magnets. The reduction of the gradient in the F magnet is to be expected from the increase of its length. The increase in the spacing between the F and D magnets causes a further reduction in the gradients of both. The consequences of these changes will be discussed in Section 2.5. Fig. 1 shows the optical functions $\sqrt{\beta_x}$, $\sqrt{\beta_y}$, and dispersion D_x . The RF cavity is at the maximum of D_x . Hence, it is possible that dangerous synchro-betatron resonances are excited.

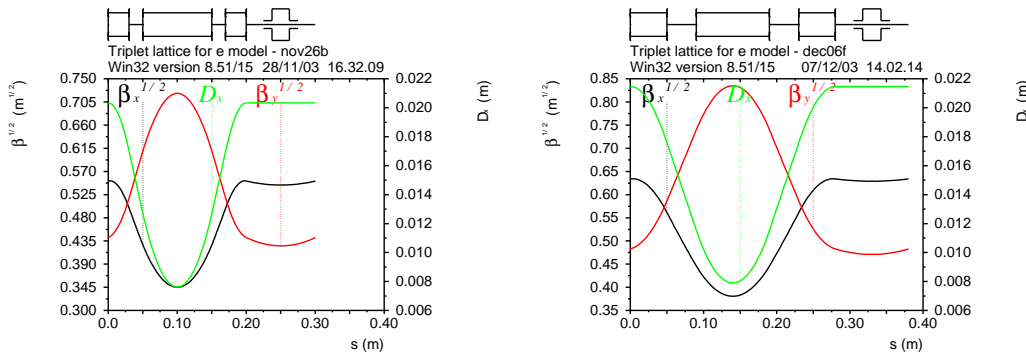


Figure 1: Orbit functions in the shorter cell on the left, the longer cell on the right

The gradients of the F and D dipoles are adjusted such that the phases advance by $q_x = 0.233$ and $q_y = 0.184$ in a lattice cell on the reference orbit at $\delta p/p = 0$. Here and in the following, q_x and q_y stand for the tunes of single cells, and Q_x and Q_y for the tunes in the whole ring. With these nominal tunes, the tunes q_x and q_y at the lower edge of the momentum range should remain well below the systematic half-integral stop band at $q = 1/2$. The bending angles in the F and D magnets are adjusted such that the flight time through a lattice cell is approximately independent of the relative momentum error to first order near $\delta p/p = 0$. All results are computed with MAD [3].

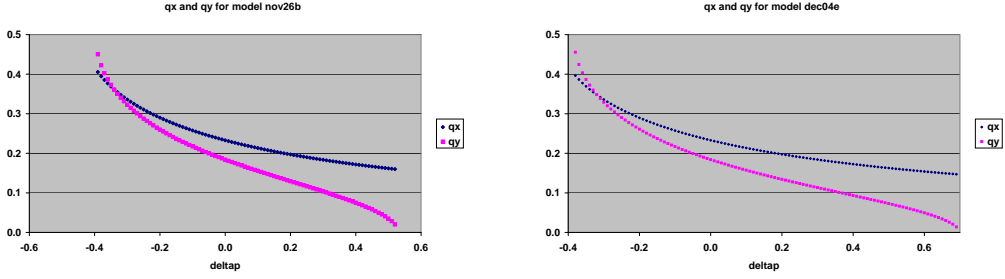


Figure 2: Variation of the tunes q_x and q_y in the shorter cell on the left, in a longer cell on the right. The abscissa is the relative momentum error $\delta p/p$. The dipoles are rectangular.

2.1 Momentum Range

Fig. 2 shows the variation of the tunes q_x and q_y with the momentum error $\delta p/p$ for a single lattice cell. The lower edge of the momentum range is caused by the vertical tune q_y approaching $1/2$ from below. The upper edge of the momentum range is caused by q_y approaching 0 from above. In the shorter cell, the betatron oscillations are stable within the momentum range $-0.39 \leq \delta p/p \leq 0.52$, while they are stable within $-0.38 \leq \delta p/p \leq 0.69$ in the longer cell.

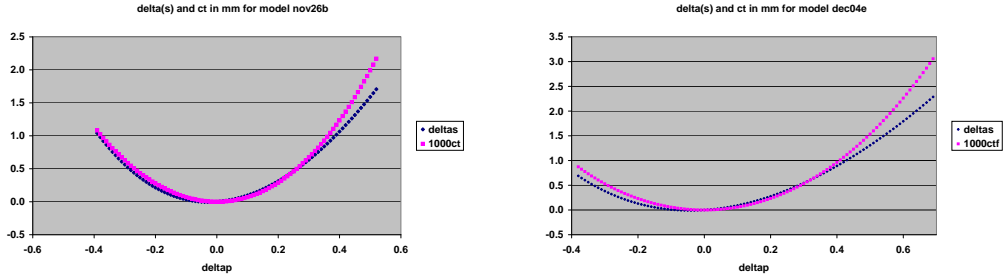


Figure 3: Variation of the orbit length δs and flight time ct in mm in a shorter cell on the left and in a longer cell on the right. The abscissa is the relative momentum error $\delta p/p$. The dipoles are rectangular.

2.2 Flight Time Spread

Fig. 3 shows the variation of the flight times with the momentum error $\delta p/p$ for a single lattice cell, and gives the results for two different calculations and two lattices. The TWISS command in MAD [3] provides those labelled $\delta(s)$, which is probably the difference in the path length between an off-momentum orbit and the reference orbit. Tracking with the TRACK command, starting on the off-momentum closed orbit, yields ct , which is probably the difference in flight time

between the off-momentum and the reference particle, multiplied by the speed of light c . Both $\delta(s)$ and ct vanish at $\delta p/p = 0$. The slope of ct at $\delta p/p = 0$ is zero by design, while that of $\delta(s)$ is almost zero. The leading variation of $\delta(s)$ and ct with $\delta p/p$ is quadratic. In the shorter cells, the spread in flight times is less than about 1 mm for $-0.37 \leq \delta p/p \leq 0.36$, while it is less than about 0.73 mm for $-0.35 \leq \delta p/p \leq 0.35$ in the longer cell. For the whole ring with 36 shorter cells, the spread in flight time is less than about 36 mm, while it is less than about 33 mm in the ring with 45 longer cells.

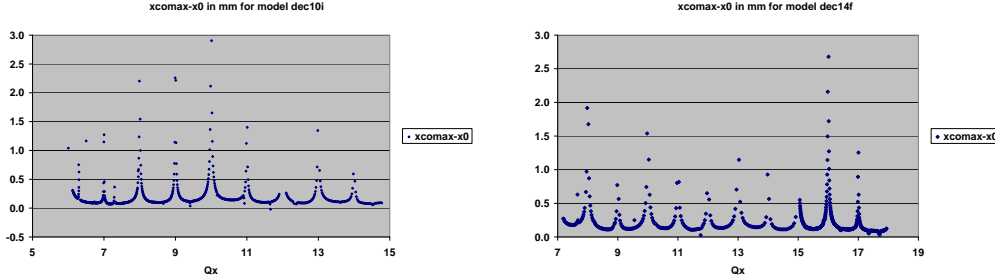


Figure 4: Maxima of the absolute values of the horizontal orbit offset $x_{\text{co}}^{\text{max}}$ in mm due to the misalignment as a function of the horizontal tune Q_x in the ring with 36 cells to the left, with 45 cells to the right. The dipole triplets are installed on girders that are displaced as a whole. Orbit offsets > 3 mm are not shown.

2.3 Misalignments

As in the earlier calculation [1] of an electron model with 33 cells, a standard deviation of 0.03 mm is adopted, and the triplets are assumed to be installed on girders that are displaced as a whole. In order to achieve this alignment tolerance, the steps assumed there are recommended. The distribution of the displacements is a Gaussian, truncated at 2.5 standard deviations. The maxima of the absolute values of the horizontal orbit offset $x_{\text{co}}^{\text{max}}$ due to the misalignment are calculated, varying $\delta p/p$ in the range $-0.396 \leq \delta p/p \leq 0.416$ for the ring with 36 cells, and $-0.382 \leq \delta p/p \leq 0.577$ for that with 45 cells, from the value printed by MAD by subtracting the maximum absolute value of the horizontal orbit offset in the perfect machine, in order to remove the contribution of the dispersion D_x and $\delta p/p$. Fig. 4 shows the result, plotted as a function of the horizontal tune Q_x . Values of $\delta p/p$ are skipped, where either the betatron oscillations are unstable in one or both planes, or where MAD does not find the closed orbit. The spikes in $x_{\text{co}}^{\text{max}}$ occur when the horizontal tune Q_x is close to an integer. By choosing the phase advance $q_x = 0.233$ and 36 or 45 cells, the horizontal tune $Q_x = 8.388$ or $Q_x = 10.485$ is far away from integral values, and the closed orbit distortions

$x_{\text{co}}^{\text{max}} = 0.106$ mm in the ring with 36 cells and $x_{\text{co}}^{\text{max}} = 0.135$ mm in the ring with 45 cells at $\delta p/p = 0$ are close to the minimum values.

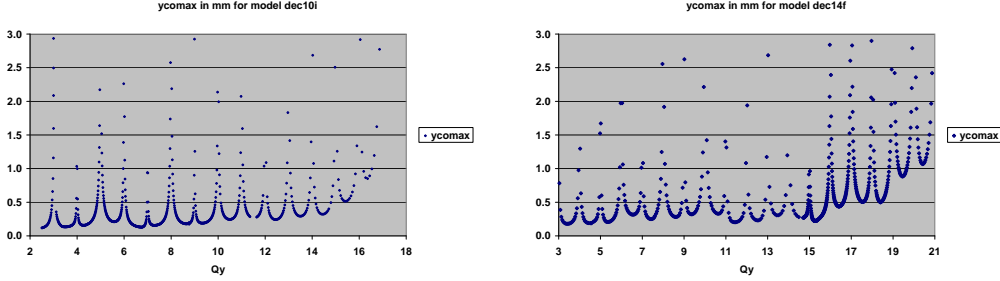


Figure 5: Maxima of the absolute values of the vertical orbit offset $y_{\text{co}}^{\text{max}}$ in mm due to the misalignment as a function of the vertical tune Q_y in the ring with 36 cells to the left, with 45 cells to the right. The dipole triplets are installed on girders that are displaced as a whole. Orbit offsets > 3 mm are not shown.

Fig. 5 shows the maxima of the absolute values of the vertical orbit offset $y_{\text{co}}^{\text{max}}$ due to the misalignment, plotted as a function of the vertical tune Q_y . Here, $y_{\text{co}}^{\text{max}}$ is printed by MAD. Values of $\delta p/p$ are skipped, where either the betatron oscillations are unstable in one or both planes, or where MAD does not find the closed orbit. The spikes in $y_{\text{co}}^{\text{max}}$ occur when the vertical tune Q_y is close to an integer. By choosing the phase advance $q_y = 0.184$ and 36 or 45 cells, the vertical tune $Q_y = 6.624$ or $Q_y = 8.280$ is far away from integral values, and the closed orbit distortion $y_{\text{co}}^{\text{max}} = 0.135$ mm in the ring with 36 cells and $y_{\text{co}}^{\text{max}} = 0.395$ mm in the ring with 45 cells at $\delta p/p = 0$ is close to the minimum value. They are much smaller than in the earlier model [1]. The momentum range in Fig. 5 is $-0.396 \leq \delta p/p \leq 0.416$ for the ring with 36 cells, and $-0.382 \leq \delta p/p \leq 0.577$ for that with 45 cells.

The integral resonances also occur for the maximum values of the dispersions D_x^{max} and D_y^{max} . Weak integral and half-integral resonances occur for the maximum values of the β -functions β_x^{max} and β_y^{max} , although there are no gradient errors in the simulation.

Figs. 6 and 7 show $x_{\text{co}}^{\text{max}}$ and $y_{\text{co}}^{\text{max}}$, respectively, for the orbits of the reference particle at $\delta p/p = 0$ due to the misalignment of the girders for 300 samples. Averaged over the samples, $\bar{x}_{\text{co}}^{\text{max}} = 0.139 \pm 0.037$ mm and $\bar{y}_{\text{co}}^{\text{max}} = 0.192 \pm 0.053$ mm are found in the ring with 36 cells. The latter is much smaller than in the earlier model [1]. Comparing these values to $x_{\text{co}}^{\text{max}} = 0.106$ mm and $y_{\text{co}}^{\text{max}} = 0.135$ mm for the first sample, used in Figs. 4, 5, 16 and 17, shows that the first sample of the ring with 36 cells is optimistic horizontally, and even more optimistic vertically. In the ring with 45 cells, $\bar{x}_{\text{co}}^{\text{max}} = 0.147 \pm 0.041$ mm and $\bar{y}_{\text{co}}^{\text{max}} = 0.266 \pm 0.083$ mm are found. Comparing these values to $x_{\text{co}}^{\text{max}} = 0.135$ mm and $y_{\text{co}}^{\text{max}} = 0.395$ mm

for the first sample, used in Figs. 4, 5, 16 and 17, shows that the first sample of the ring with 45 cell is close to the average behaviour horizontally, and pessimistic vertically.

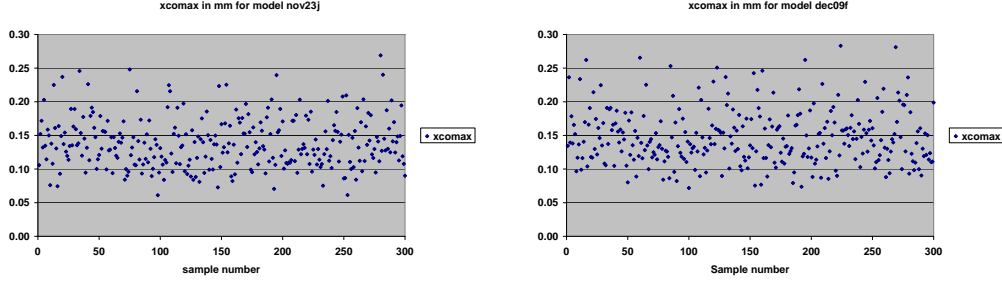


Figure 6: Maxima of the absolute values of the horizontal orbit offset x_{CO}^{\max} in mm for the reference particle at $\delta p/p = 0$ due to the misalignment for 300 samples in the ring with 36 cells to the left, with 45 cells to the right. The triplets are displaced as a whole. Rectangular dipoles are assumed.

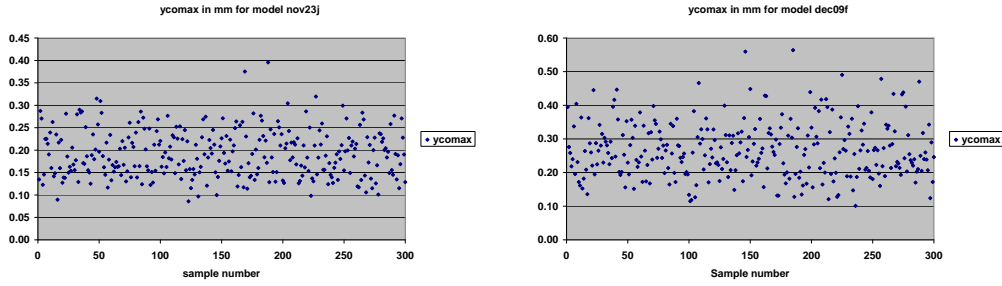


Figure 7: Maxima of the absolute values of the vertical orbit offset y_{CO}^{\max} in mm for the reference particle at $\delta p/p = 0$ due to the misalignment for 300 samples in the ring with 36 cells to the left, with 45 cells to the right. The triplets are displaced as a whole. Rectangular dipoles are assumed.

Figs. 8 and 9 show the maximum absolute values of horizontal dispersion D_x and vertical dispersion D_y , respectively, for the orbits of the reference particle at $\delta p/p = 0$ due to the misalignment of all girders as a whole for 300 samples. Rectangular dipoles are assumed. Averaging over the samples in the ring with 36 cells, $\bar{D}_x = 22 \pm 0.63$ mm, compared to $D_x = 20.3$ mm in the perfect ring, and $\bar{D}_y = 4.2 \pm 1.6$ mm are found. The vertical dispersion \bar{D}_y is much smaller than in the earlier model [1]. Comparing these values to $D_x = 21.7$ mm and $D_y = 2.1$ mm for the first sample, used in Figs. 4, 5, 16 and 17, shows that the ring with 36 cells is optimistic horizontally, and even more optimistic vertically. In the ring with 45 cells, $\bar{D}_x = 23.5 \pm 0.732$ mm, compared to $D_x = 21.5$ mm in

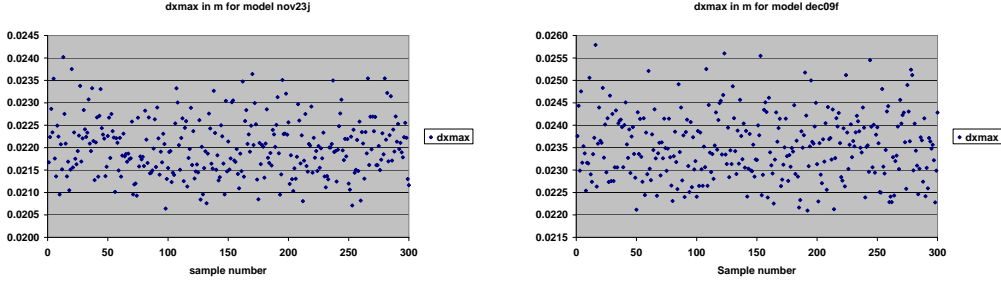


Figure 8: Maxima of the absolute values of the horizontal dispersion D_x in m for the reference particle at $\delta p/p = 0$ due to the misalignment for 300 samples in the ring with 36 cells to the left, with 45 cells to the right. All triplet+s are displaced as a whole. Rectangular dipoles are assumed.

the perfect ring, and $\bar{D}_y = 8.93 \pm 4.20$ mm are found. Comparing these values to $D_x = 23.8$ mm and $D_y = 16.5$ mm for the first sample, used in Figs. 4, 5, 16 and 17, shows that the ring with 45 cells is close to average horizontally plane, and pessimistic vertically.

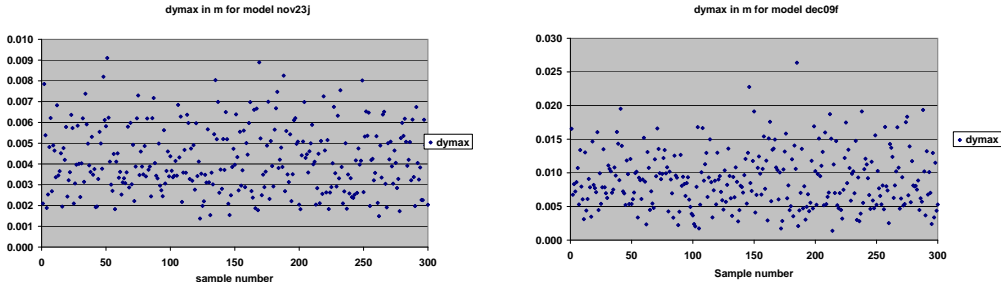


Figure 9: Maxima of the absolute values of the vertical dispersion D_y in m for the reference particle at $\delta p/p = 0$ due to the misalignment for 300 samples in the ring with 36 cells to the left, with 45 cells to the right. All girders are displaced as a whole. Rectangular dipoles are assumed.

2.4 Aperture

In order to compute the half apertures A_x and A_y , one needs the maxima of the absolute value of the orbit offset $|x_c|$, and of the β -functions β_x^{\max} and β_y^{\max} as functions of the relative momentum error $\delta p/p$, provided by MAD [3], as well as parameters of the injected beam. Tab. 2 gives them for the ATF [4] at BNL, and the injector for CTF3 [5] at CERN. They are not necessarily optimised injectors for electron models of FFAG rings.

Table 2: Typical Parameters of Electron Beams

Parameter	ATF	CTF	
Beam energy	≤ 72	20	MeV
Normalised transverse emittance	10^{-3}	10^{-4}	rad m
Normalised longitudinal emittance	$2 \cdot 10^{-7}$	10^{-6}	eVs
Bunch charge	0.5	1	nCb

To find the contribution of the betatron oscillations to the aperture, a normalised RMS emittance $\varepsilon_n = 0.3$ mm of the electron beam is assumed, and 3 RMS beam radii are allowed for in the half aperture. Here, ε_n is defined as the product of the RMS beam radius σ and RMS transverse momentum $\Delta p/p_0$ in units of the muon rest momentum p_0 . The figure $\varepsilon_n = 0.3$ mm is the geometric mean between the figures in Tab. 2. In the horizontal plane, the betatron beam size is added to the orbit offset $|x_c|$. Fig. 10 shows the half apertures A_x and A_y thus obtained as functions of the relative momentum error $\delta p/p$. It may be seen that a vertical aperture radius $A_y \approx 10.5$ mm and a horizontal aperture radius $A_x \approx 14.4$ mm are needed in the ring with 36 cells, and $A_y \approx 10.7$ mm and $A_x \approx 15.3$ mm in the ring with 45 cells, both for a momentum range $-0.35 < \delta p/p < +0.35$. This method of combining the maximum values of orbit offset $|x_c|$ and β -functions β_x^{\max} and β_y^{\max} surely overestimates the vertical aperture A_y of the F magnets and the horizontal aperture A_x of the D magnets, and the magnetic field at the edge of the aperture in the D magnets.

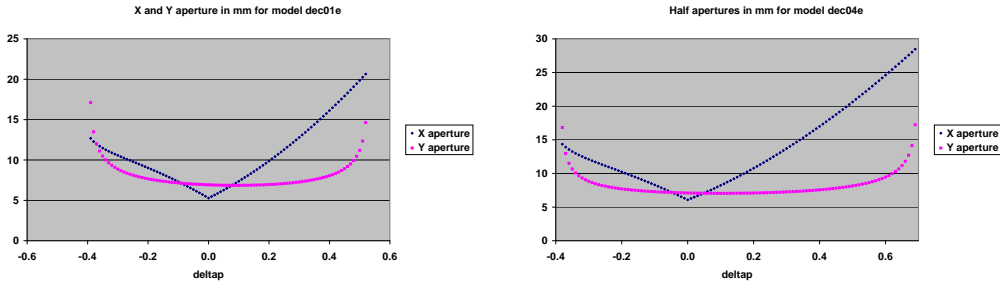


Figure 10: Horizontal and vertical half apertures in mm of a cell with rectangular dipoles as functions of the relative momentum error $\delta p/p$ for ring with 36 cells to the left, with 45 cell to the right

2.5 Practical Lattice Considerations

Tab. 3 shows a summary of the lattice considerations for the two rings. The ratio of magnetic field and gradient B/G is the characteristic length, i.e. the lateral distance between the reference orbit and the radius where the magnetic field vanishes. Allowing a few mm for closed orbit distortions, in addition to the aperture radii calculated in Section 2.4, yields the horizontal and vertical aperture radii A_x and A_y , respectively. In the F magnets, B/G is smaller than the horizontal aperture radius A_x . Hence, they are assumed to be displaced quadrupoles, rather than C or H shaped gradient dipoles. In the D magnets, $B/G \approx 23.5$ mm is larger than the horizontal aperture radius A_x . Hence, they are assumed to be half quadrupoles with a neutral pole. With respect to the centre of the quadrupole, where $B = 0$, the horizontal aperture is in the ranges of x shown in Tab. 3. Assuming that the hyperbolic pole face passes through the point with the largest value of x and $y = A_y$, yields the bore radius r , and the pole tip field $B(r)$, by using the gradients in Tab. 1, using

$$I = \frac{rB(r)}{2\mu_0} \quad (1)$$

for the current I flowing around one pole in a steel-conductor quadrupole, in the absence of saturation. The number of turns is a matter of the magnet optimization.

Table 3: Field and Aperture Parameters

Magnet	F		D		
Cells	36	45	36	45	
B/G	8.4	6.6	23.5	22.6	mm
A_x	± 18	± 19	± 18	± 19	mm
A_y	± 12	± 12	± 12	± 12	mm
x	-9.6 ... 26.4	-12.4 ... 25.6	5.5 ... 41.5	3.6 ... 41.6	mm
r	25.2	24.8	31.6	31.6	mm
$B(r)$	0.32	0.14	0.20	0.15	T
I	3209	1381	2515	1886	A

2.5.1 RING WITH 36 CELLS

The QL3 quadrupoles in the CTF3 test facility at CERN have gradient 11.2 T/m, bore radius 29 mm, quite similar to the F magnets in the ring with 36 cells, but are much longer with yoke length 0.2 m. The cost of 14 QL3 quadrupoles was about 200 kCHF in early 2003. Comparing their effective magnetic length 0.226 m to

their overall length including coil overhangs 0.287 m shows that one coil overhang is about 30 mm, while the lattice design allows about 20 mm for the coil overhangs of two neighbouring magnets. A coil design with two layers would reduce the coil overhang by about 10 mm, and increase the transverse size of the quadrupole from 282 mm to about 302 mm. The aperture and good field region in the D magnets extend well beyond the circle inscribed between the poles.

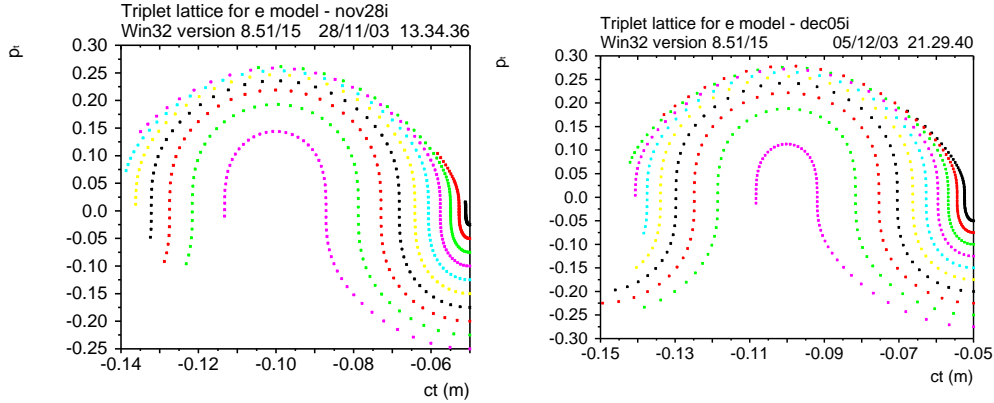


Figure 11: Acceleration in a perfect ring consisting of 36 cells to the left and 45 cells to the right with rectangular dipoles and $V = 20$ kV accelerating voltage without alignment errors. The graphs show the longitudinal phase space (ct, p_t) . Coordinates are recorded every $1/3$ of 18 turns. $V = 0$ at $ct = -0.15, -0.10, -0.05$ m. V reaches the maximum at $ct = -0.075$ m, and the minimum at $ct = -0.125$ m.

2.5.2 RING WITH 45 CELLS

Tab. 1 shows that most of the magnet parameters in the ring with 45 cells are quite similar to those in the ring with 36 cells. The pole tip fields $B(r)$ are the exception, and $B(r)$ is more than a factor of two smaller in the F magnets, and still 25% smaller in the D magnets. This is more than expected from the increase of the length of the F magnets. This reduction of $B(r)$ and the associated reduction of the current I allow two options.

- The pole tip field $B(r)$ is only a little higher than that achieved in the quadrupoles of the Recycler at Fermilab [6]. Permanent quadrupoles should be seriously considered for this electron model with 45 cells. The maximum achievable $B(r)$ should be investigated, and if needed, a small reduction in the accelerating range of the model should be foreseen. It would be of the order of 10%, much smaller than the factor of two proposed earlier [1].

- Steel-conductor quadrupoles similar to QL3 could be built with the coils in a single layer. Compared to QL3, this would reduce the two neighbouring coil overhangs to about 30 mm, shorter than the 40 mm drift space.

3 Acceleration

Because of the vanishing slope of ct and $\delta(s)$ at $\delta p/p = 0$, the FFAG rings have transition at the reference energy, and there are no buckets. Nevertheless, electrons are accelerated. Following the notation in MAD [3], the longitudinal coordinate $\delta p/p$ is called p_t in this chapter. Acceleration over a substantial range in p_t is considered. The tunes change by several integers. Hence, several integral resonances are crossed.

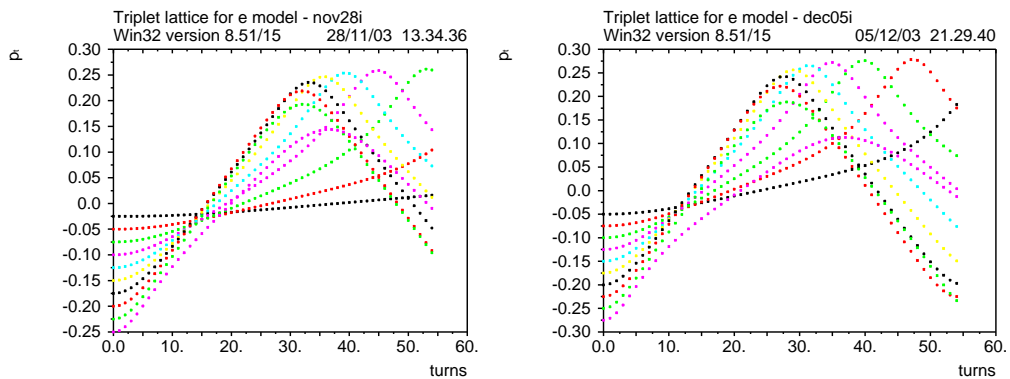


Figure 12: Acceleration in a perfect ring consisting of 36 cells to the left and 45 cell to the right with rectangular dipoles and 20 kV accelerating voltage without alignment errors. The graphs show the relative momentum error p_t vs. "turns". The abscissa "turns" is labelled in units of 1/3 of a turn.

3.1 Longitudinal Simulation in a Perfect Model

Figs. 11 and 12 show the motion in longitudinal phase for particles, launched below the unstable fixed point at $ct = -50$ mm with $-0.250 \leq p_t \leq -0.025$ in the lattice with 36 cells, and with $-0.275 \leq p_t \leq -0.025$ in the lattice with 45 cells, and tracked for 18 turns at 20 kV accelerating voltage. They reach their maximum p_t at $ct = -100$ mm, above the neighbouring stable fixed point. Particles launched at $ct = -50$ mm with $p_t \leq -0.275$ in the lattice with 36 cells, and with $p_t \leq -0.3$ in the lattice with 45 cells are either unstable or remain below $p_t = 0$, and are not shown. The initial and final momenta do not have equal magnitude and opposite sign. Electrons launched with lower p_t remain at lower p_t . The maximum acceleration is about 0.4 units of p_t , or from about 12 to about 18 MeV, in the ring

with 36 cells, and about 0.5 units of p_t , or from about 11.25 to 18.75 MeV, in the ring with 45 cells. Details are in the figure caption.

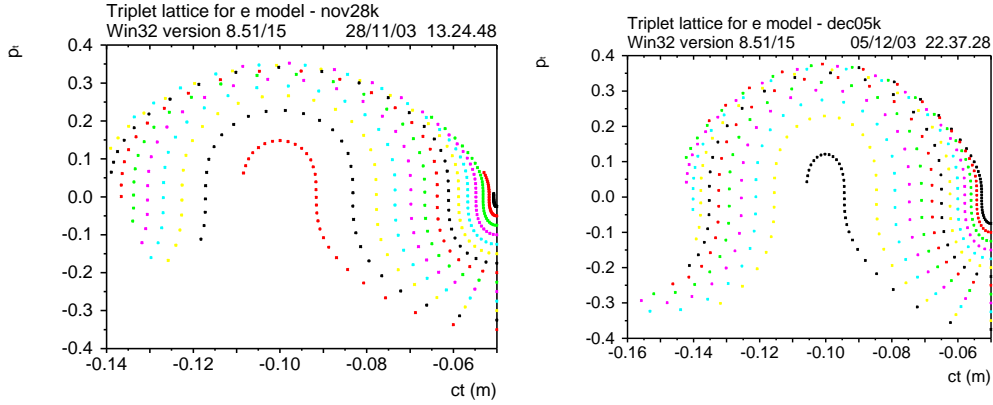


Figure 13: Acceleration in a perfect ring consisting of 36 cells to the left and 45 cells to the right with rectangular dipoles and $V = 50$ kV accelerating voltage without alignment errors. The graphs show the longitudinal phase space (ct, p_t). Coordinates are recorded every $1/3$ of 10 turns. $V = 0$ at $ct = -0.10, -0.05$ m. V reaches the maximum at $ct = -0.075$ m, and the minimum at $ct = -0.125$ m.

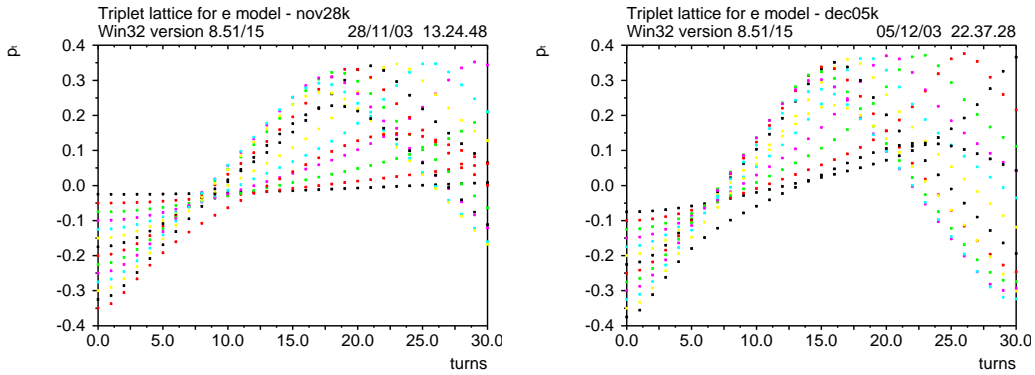


Figure 14: Acceleration in a perfect ring consisting of 36 cells to the left and 45 cell to the right with rectangular dipoles and 50 kV accelerating voltage without alignment errors. The graphs show the relative momentum error p_t vs. "turns". The abscissa "turns" is labelled in units of $1/3$ of a turn.

Figs. 13 and 14 are similar to Figs. 11 and 12, respectively. The accelerating voltage is 50 kV. Particles launched with $-0.350 \leq p_t \leq -0.025$ and with $-0.375 \leq p_t \leq -0.025$ are accelerated in the lattice with 36 and 45 cells, respectively. The range of acceleration increases from about 0.4 at 20 kV to about 0.5 units of p_t at 50 kV accelerating voltage.

3.2 Longitudinal Phase Space

These simulation results can be understood by inspecting the longitudinal Hamiltonian H_1 in the variables φ and p_t [7]:

$$H_1 = h \left(\frac{\eta_0 p_t^2}{2} + \frac{\eta_1 p_t^3}{3} + \frac{\eta_2 p_t^4}{4} + \dots \right) + \frac{eV N_c}{2\pi\beta_0^2 E_0} [\cos(\varphi_s + \varphi) + \varphi \sin \varphi_s] \quad (2)$$

Here, h is the harmonic number, V is the accelerating RF voltage in one of N_c cavities, φ_s is the stable phase angle, counted from the last zero crossing of the RF wave form, and β_0 and E_0 are speed in units of the light velocity and energy of the reference particle, respectively. The coefficients η_i are the slip factor η_0 and its higher order terms. In electron models which are operated with the reference energy equal to transition energy, $\eta_0 = 0$. Ignoring the terms proportional to η_i with $i \geq 2$, the Hamiltonian H_2 becomes much simpler:

$$H_2 = \frac{2\pi\beta_0^2 E_0 h \eta_1 p_t^3}{3eV N_c} + [\cos(\varphi_s + \varphi) + \varphi \sin \varphi_s] \quad (3)$$

All parameters are assembled in the first term of (3) which may be taken as the cube of a scaled momentum variable y :

$$y = p_t \left(\frac{2\pi\beta_0^2 E_0 h \eta_1}{3eV N_c} \right)^{1/3} \quad (4)$$

Fig. 15 shows a contour plot of $H_2(\varphi, y)$. Acceleration along the bright blue band has the property that initial and final y have the same magnitude $|y| = 1$ and opposite sign, as is appropriate for accelerating from 10 to 20 MeV at 15 MeV reference energy, or from $p_t = -1/3$ to $p_t = +1/3$. Solving (4) with $|y| = 1$ for p_t yields the acceleration range for given parameters, and explains why increasing the RF voltage by a factor 2.5 between Figs. 11 and 13 increases the acceleration range by only a factor $2.5^{1/3} \approx 1.36$:

$$p_t = \left(\frac{3eV N_c}{2\pi\beta_0^2 E_0 h \eta_1} \right)^{1/3} \quad (5)$$

The circumferential accelerating voltage, ranging from $20 \times 36 = 0.72$ MV to $50 \times 48 = 2.25$ MV, is a substantial fraction of the reference energy 15 MeV. Hence, the changes of p_t from turn to turn are substantial, as can be seen in Figs. 11 and 13, and the number of turns needed to reach the final p_t is small, between 5 and 11.

The circumferential RF voltage $N_c V$ in (5) is proportional to the cube of the accelerating range p_t , the harmonic number h , or the frequency f_{RF} , and the coefficient η_1 , or the spread in flight times shown in Fig. 3. For given range p_t , the easiest way of reducing $N_c V$, or of making more efficient use of the RF system, and increasing the number of turns, is reducing h or η_1 or both.

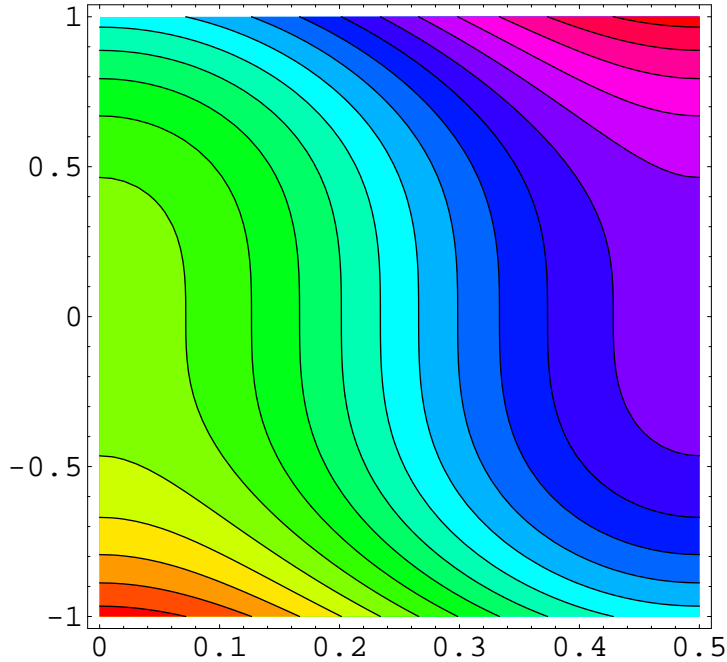


Figure 15: Contour plot of the longitudinal Hamiltonian $H_2(\varphi, y)$ in (3). The phases $\varphi_s = 1/2$ and φ are measured in cycles. The abscissa is φ . The ordinate is the scaled momentum variable y , defined in (4). H_2 is symmetrical around $\varphi = 0$ and has period one in φ .

3.3 Longitudinal Simulation in a Model with Alignment Errors

Fig. 16 shows the consequences of misalignments on the acceleration of particles. The triplets are installed on girders, which are displaced with 0.03 mm standard deviation, as in the first sample of the random displacements in Figs. 6 to 9. The accelerating voltage is 50 kV in each cavity as in Figs. 13 and 14. Comparing Figs. 16 and 17 to Figs. 13 and 14 shows very similar behaviour, apart from the factor of three in the number of observations. However, it should be remembered that this simulation was done for individual particles, and not for bunches with finite emittances in all three degrees of freedom.

3.4 Practical RF Considerations

The slip factor η_1 is a lattice parameter that is used in (2), (3), (4), and (5). It can be obtained from the flight times shown in Fig. 3. RF cavities are installed

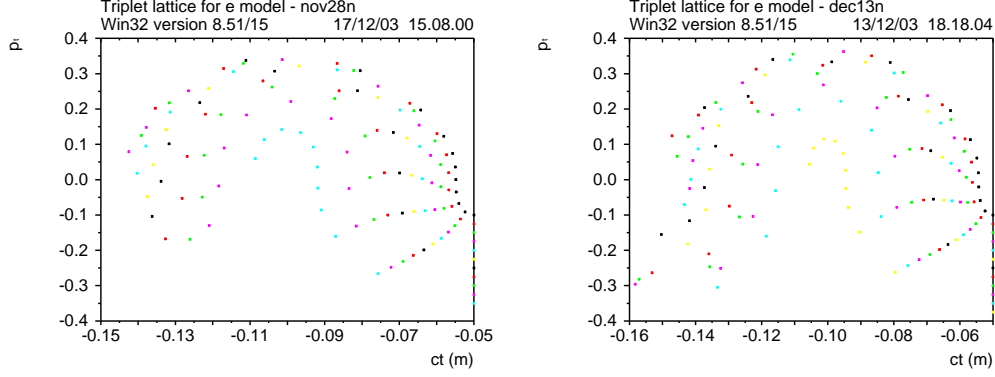


Figure 16: Acceleration in a ring consisting of 36 cells to the left and 45 cell to the right with rectangular dipoles and $V = 50$ kV accelerating voltage. The dipoles are installed on girders which are displaced with 0.03 mm standard deviation. The graphs show the longitudinal phase space (ct, p_t) . $V = 0$ at $ct = -0.15, -0.10, -0.05$ m. V reaches the maximum at $ct = -0.075$ m, and the minimum at $ct = -0.125$ m.

in all lattice cells. The total circumferential voltage is the product of the number of RF cavities and the accelerating voltage V in a cavity. The peak voltage in the RF cavities U is larger than the accelerating voltage V by the reciprocal of the transit time factor which is $2/\pi$ in a cavity of length $\lambda_{\text{RF}}/2$. The RF cavities have the shape of a pillbox, and are made of copper with conductivity $\sigma = 5.8 \times 10^7 \Omega^{-1}\text{m}^{-1}$. Their intrinsic impedance is $R/Q = 121 \Omega$, their quality factor is $Q = 17733$. The beam ports are neglected, and the calculation follows [8]. The RF power P needed in each RF cavity is:

$$P = \frac{U^2}{2Q(R/Q)} = \frac{\pi^2}{8} \frac{V^2}{Q(R/Q)} \quad (6)$$

The beam loading of the RF cavities can be estimated, comparing the energy extracted by the beam W_e to the stored energy W_s in the cavity, which is given by:

$$W_s = \frac{U^2}{4\pi f_{\text{RF}}(R/Q)} \quad (7)$$

Here $f_{\text{RF}} \approx 3$ GHz is the frequency of the RF system. With total beam current I and acceleration within n turns, the extracted energy W_e by all bunches and during all turns is

$$W_e = VnIh/f_{\text{RF}} \quad (8)$$

Here, e is the electron charge, and h is the harmonic number of the RF system. Requiring $W_e \ll W_s$, and solving for I yields an upper limit:

$$I \ll \frac{\pi V}{16nh(R/Q)} \quad (9)$$

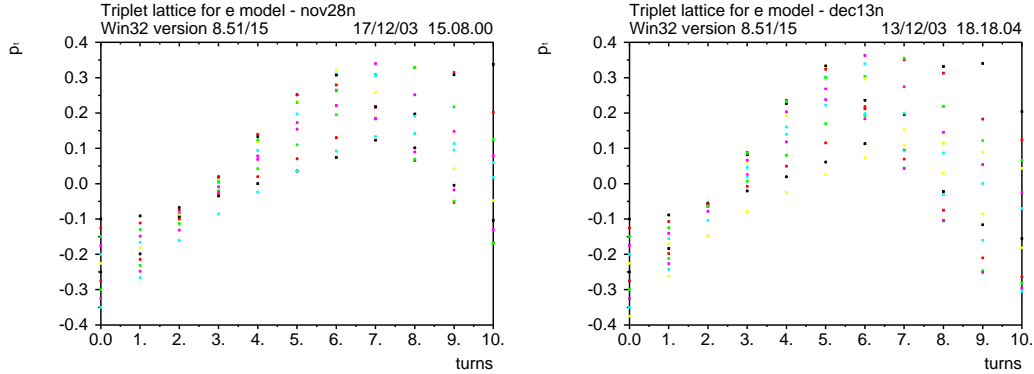


Figure 17: Acceleration in a ring consisting of 36 cells to the left and 45 cell to the right with rectangular dipoles and 50 kV accelerating voltage. The dipoles are installed on girders which are displaced with 0.03 mm standard deviation. The graphs show the relative momentum error p_t vs. turns.

The limits for I displayed in Tab. 4 show that beam loading is severe. It depends on the total beam current I , but not on the number of bunches k which can be chosen freely in the range $1 \leq k \leq h$. Arguments entering into the choice are the bunch charge available from the injector, gaps between bunches for kicker rise and fall times, and the beam observation system, which must work to the expected accuracy at the bunch current I/k . An accurate calculation of transient beam loading, taking into account the variation of phase and acceleration in Figs. 11, 13 and 16 is beyond the scope of this note.

Typical buncher cavities in S band linacs are very similar to the RF cavities envisaged here. All RF cavities can be fed from a single CW power source, probably a travelling wave tube, with a single waveguide around the circumference of the ring, equipped with couplers that tap off the appropriate amount of RF power at every RF cavity. Whether to install RF cavities in all cells, or only every so often, is related to beam loading, which gets alleviated with fewer cavities at a higher voltage and power, the optimisation of the RF system, and the space needed for other equipment, e.g. injection and ejection kickers. Tab. 4 lists the parameters related to acceleration and the RF system, derived in this chapter.

3.5 Variants of Acceleration

The discussion so far concentrated on the acceleration over the full momentum range, about a factor of two, starting below a fixed point, where the RF voltage crosses zero, and ending at the neighbouring fixed point, where the RF voltage also crosses zero, as shown in Figs. 11, 13, and 16. This scheme has two disadvantages: (i) Acceleration is rather slow, and the integral resonances are crossed

Table 4: RF System Parameters

Slip factor η_1	0.0227	0.0227	0.0149	0.0149	
Number of cavities N_c	36	36	45	45	
Harmonic number h	108	108	171	171	
Accelerating voltage V	20	50	20	50	kV
Peak RF voltage U	31.4	78.5	31.4	78.5	kV
RF power P	230	1440	230	1440	W
Stored energy W_s	0.216	1.35	0.216	1.35	mJ
Initial p_t	-0.2089	-0.2816	-0.2233	-0.3011	
Final p_t	0.2088	0.2815	0.2234	0.3012	
Number of turns n	11	6	9	5	
Beam current I	$\ll 27.3$	$\ll 125$	$\ll 21.1$	$\ll 94.9$	mA

rather slowly, soon after the beginning and just before the end of acceleration; (ii) The rate of acceleration through the resonances is fixed. The first disadvantage can be avoided by increasing the RF voltage, launching the injected beam at $ct \approx -0.0625$ m and extracting it at $ct \approx -0.0875$ m. The second disadvantage can be avoided for resonances close to $\delta p/p \approx 0$ by reducing range and speed of resonance crossing, operating the model at smaller RF voltage.

4 Conclusions

Parameters are derived for the lattice and RF system of two electron models of a non-scaling FFAG ring, accelerating electrons from about 10 to 20 MeV. Lattice parameters such as magnet types and dimensions, spacings, and number of cells are presented. The models have about 10 metres and 17 metres circumference. The magnet aperture radii are about 12 mm \times 18 mm. The tune variation with momentum is similar to that in a full machine, and would allow the study of resonance crossing. The variation of orbit length with momentum is less than 36 mm, and would allow the study of acceleration outside a bucket. A 100 mm straight section, in each cell, is adequately long for an RF cavity that operates at 3 GHz and is half an RF wavelength long. The accelerating voltage needed is calculated. Practical RF system design issues, e.g. RF power, and the limit on the bunch population due to beam loading are estimated.

Compared to the earlier model [1] the number of periods was increased from $33 = 3 \times 11$ to $36 = 2^2 \times 3^2$ and $45 = 3^2 \times 5$. This provides more flexibility in the choice of the number of RF cavities, etc. The nominal tunes at $\delta p/p = 0$, $Q_x =$

8.388 or 10.485 and $Q_y = 6.624$ or 8.280 , are well away from integral values, and the response of vertical closed orbit and vertical dispersion to misalignments is much improved. Increasing the number of cells increases the ranges of tunes Q_x and Q_y from injection to final energy, and hence the number of resonances that have to be crossed. In the model with 45 cells the magnetic fields are much smaller than in that with 36 cells. The magnets can be either conventional steel-conductor quadrupoles or permanent-magnet quadrupoles [6].

The RF system operates at about 3 GHz. Acceleration over a range $\pm p_t$ is studied in a Hamiltonian formalism and by simulation with transition at the reference energy E_0 . It is found that E_0 , range $\pm p_t$, lattice parameter η_1 , circumferential accelerating RF voltage $N_c V$, and harmonic number h are related by the rather fundamental equation (5). In the models, $N_c V$ is between 0.72 and 2.25 MV, a substantial fraction of the range 10 MeV, and the number of turns is between 5 and 11. The upper limit on the total beam current due to beam loading of the RF system is severe.

The simulation techniques presented can be applied not only to electron models, but also to FFAG rings accelerating muons.

Acknowledgements

I should like to thank Andy Sessler for encouragement and critical readings, the participants in the recent FFAG workshop at BNL for stimulating discussions, and R. Corsini, G. Geschonke, W. Kalbreier, M. Mayoud, L. Rinolfi and T. Zickler at CERN for helpful advice.

References

- [1] E. Keil and A.M. Sessler, CERN-AB-2003-095 (ABP) (2003).
- [2] J.S. Berg BNL, private communication (Oct 2003).
- [3] H. Grote and F.C. Iselin, CERN SL/90-13 (AP) Rev.4 (1995).
- [4] I. Ben-Zwi BNL, private communication (Dec 2003).
- [5] H. Braun et al., Proc. 20th Internat. Linac Conf., Monterey CA 2000.
- [6] E. Keil, CERN-SL/2000-006 (AP) (2000).
- [7] K.Y. Ng, in Handbook of Accelerator Physics and Engineering, eds. A.W. Chao and M. Tigner, 2nd printing (Singapore 2002) 94.
- [8] W. Schnell, in Handbook of Accelerator Physics and Engineering, eds. A.W. Chao and M. Tigner, 2nd printing (Singapore 2002) 526.